Mandible bone mineral density estimation using spectral panoramic X-ray imaging

Villeseveri Somerkivi(ID)[1,2,3], Thorsten Sellerer(ID)[1,2], Daniel Berthe(ID)[1,2], York Haemisch(ID)[4],
Tuomas Pantsar(ID)[4], Henrik Lohman(ID)[4], Touko Kaasalainen(ID)[5], Franz Pfeiffer(ID)[1,2,6,7,*]

[1]*Department of Physics, School of Natural Sciences, Technical University of Munich, Garching, Germany*
[2]*Munich Institute of Biomedical Engineering, Technical University of Munich, Garching, Germany*
[3]*Planmeca Oy, Helsinki, Finland*
[4]*Varex Imaging Corporation, Salt Lake City, USA*
[5]*HUS Diagnostic Center, University of Helsinki and Helsinki University Hospital, Finland*
[6]*Department of Diagnostic and Interventional Radiology, Klinikum Rechts der Isar, Munich, Technical University of Munich, Germany*
[7]*Institute for Advanced Study, Technical University of Munich, Garching, Germany*

ABSTRACT

Purpose: This study demonstrated the feasibility of obtaining mandible bone mineral density (BMD) scores using spectral panoramic imaging.

Materials and Methods: Areal BMD scores were measured from the body and angle of the mandible in 3 anthropomorphic head phantoms using a spectral panoramic system (Planmeca Promax Mid, Planmeca Oy, Helsinki, Finland) equipped with a DC-Vela detector (Varex Imaging Corporation, Salt Lake City, USA). These results were compared to synthetic panoramic images generated from dual-energy CT acquisitions. Reproducibility was evaluated by repeatedly scanning 1 phantom with minor patient positioning errors, and the linearity of the BMD scores was assessed using calcium inserts in a Gammex 472 phantom (Sun Nuclear, Melbourne, USA).

Results: The experimental and synthetic panoramic images appeared visually similar. The mean synthetic score was $0.640 \, g/cm^2$, and the anthropomorphic phantoms produced a root mean squared error of $0.0292 \, g/cm^2$ with a correlation coefficient of 0.969. Typical patient positioning errors did not substantially increase the error, which measured $0.0296 \, g/cm^2$ and $0.0474 \, g/cm^2$ for the left and right sides, respectively. Linearity tests using the Gammex phantom yielded a correlation coefficient of 0.998 for BMD scores ranging from 0.03 to $2.7 \, g/cm^2$.

Conclusion: The BMD data obtained from spectral panoramic imaging are consistent with both dual-energy CT and Gammex phantom measurements. Consequently, spectral panoramic imaging shows potential as a method for osteoporosis screening, leveraging the widespread use of panoramic imaging. *(Imaging Sci Dent 2025; 55: 56-64)*

KEY WORDS: Radiography, Dual-Energy Scanned Projection; X-Rays; Bone Density

Introduction

Osteoporosis affects at least 200 million people worldwide,[1] and it is responsible for over 1 million fractures annually in the United States alone.[2,3] In addition, osteoporosis increases the risk of dental implant failure[4] and periodontal disease.[5] Early detection of osteoporosis enables treatment with dietary supplements and increased physical activity.[6]

Bone mineral density (BMD) is a key indicator of osteoporosis and is most commonly measured at the lumbar spine using dedicated dual-energy X-ray absorptiometry (DXA) systems.[7] However, BMD can also be assessed at other anatomical sites, reflecting overall bone health.[5] Mandibular BMD, in particular, correlates significantly with measurements taken at the forearms and lumbar spine,[8,9] and serves as an important marker of skeletal health. Although dedicated mandibular DXA scanners have been available for several decades,[5,8] they are not widely used clinically.

Instead, mandible health is typically evaluated through visual assessment of panoramic images acquired via dental panoramic X-ray imaging—a low-dose and widely available modality in dental clinics.[10] BMD can also be measured from the extremities and mandible using cone beam computed tomography (CT),[11] and approximately the same number of panoramic and CT images are acquired worldwide each year.[12]

The newly developed technique of spectral panoramic X-ray imaging enables obtaining quantitative measurements of soft tissue and bone thickness.[13] The resulting bone thickness images may be well-suited for estimating BMD from panoramic images. If BMD estimation can be successfully integrated into these systems, it could enable the generation of substantial, clinically relevant BMD data without increasing radiation exposure or complicating existing workflows.

This study evaluated the feasibility of spectral panoramic imaging for generating BMD maps of the mandible. Reference data were obtained from a clinical dual-energy computed tomography (DECT) scanner, and a simulation framework from previous work[14] was adapted to produce basis material panoramic images from decomposed DECT volumes. Experimental basis material images were then compared to their synthetic reference counterparts to assess the suitability of the spectral imaging approach.

Materials and Methods

Phantoms

A total of 3 anthropomorphic head phantoms, each containing a real human skull encased in plastic, were used in this study. Two of these were RANDO SK150 phantoms (Radiation Analogue Dosimetry System; The Phantom Laboratory, Salem, NY, USA), and the third was an X-ray Phantom Head (Erler-Zimmer GmbH, Lauf, Germany). The 2 RANDO SK150 phantoms feature air holes in the plastic that mimic the upper respiratory tract; one (labeled 1) has a drilled hole in the mandible, while the other (labeled 2) does not, as shown in Figure 1A. The X-ray Phantom Head (labeled 3) contains no air gaps in its plastic construction.

To assess the linearity of the BMD scores, the Gammex 472 dual energy phantom (Sun Nuclear, Melbourne, FL, USA) was used. This phantom contains inserts with calcium concentrations of 50, 100, 200, 300, 400, 500, and 600 mg/mL, each with a diameter of 2.85 cm. Calcium, being the heaviest element in the bone mineral hydroxyapatite (HAP: $Ca_5(PO_4)_3OH$), is critical for these measurements. A solid water insert served as the reference. Additionally, 10 cm of polymethyl methacrylate (PMMA) slabs were stacked in the background to simulate the soft tissue component of the head phantoms. The measurement configuration is illustrated in Figure 1B, and a region of interest (ROI) measuring 100 pixels in height by 200 pixels in width was used to measure the aBMD over the cylindrical inserts.

For the head phantoms, the optimal area for areal BMD (aBMD) measurement was the mandibular body, located below the molar and canine teeth.[6] This site is anatomically stable across patients, making it particularly relevant for comparative aBMD assessments, and it exhibits the highest correlation with aBMD values at other skeletal sites.[8] Specifically, a measurement was taken from the entire mandible region beneath the second premolar, first molar, and second
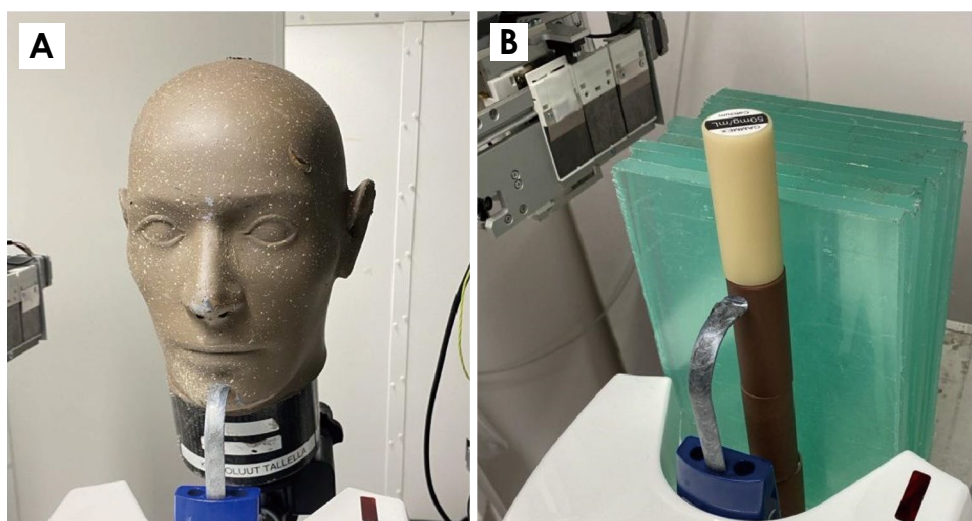

Fig. 1. A. Anthropomorphic head phantom number 2: RANDO SK150 (Radiation Analogue Dosimetry System; The Phantom Laboratory, Salem, NY, USA). B. Gammex dual-energy inserts (Sun Nuclear, Melbourne, FL, USA) with the PMMA background.
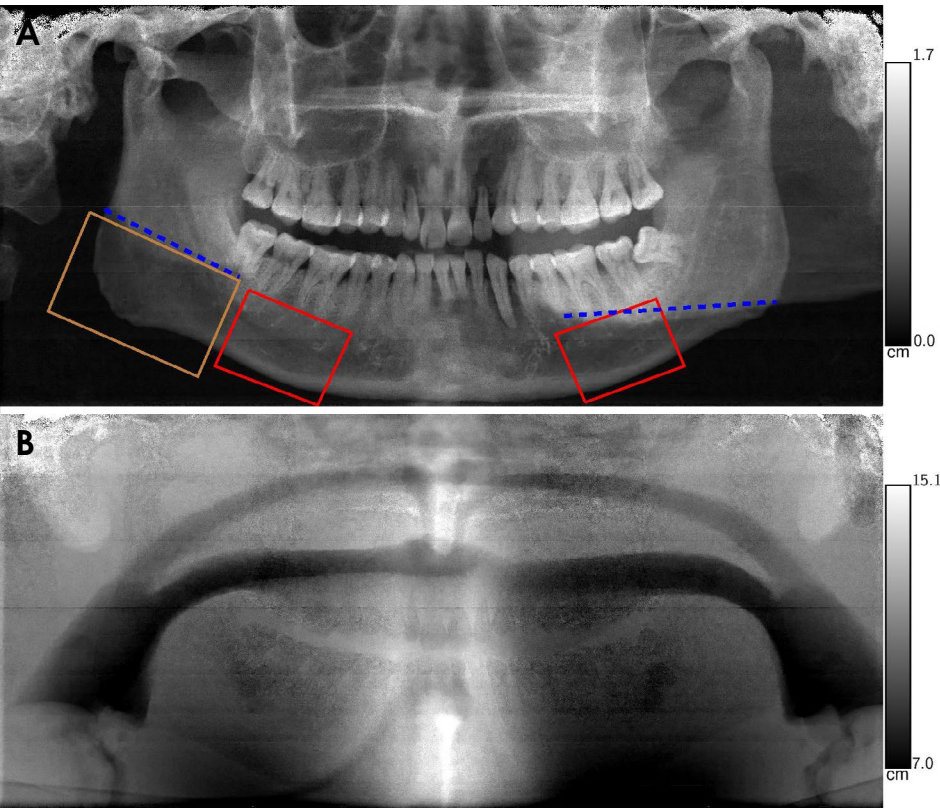
Fig. 2. A. Dentin component obtained from the spectral panoramic system. The rectangles highlight the area used for the aBMD measurement—red for the mandibular body and brown for the angle of the mandible. The blue dashed line highlights the lower border of the opposing mandible overlap region, which precludes measurement of the right mandibular angle. B. Soft tissue component obtained from the spectral panoramic system.

molar (see Fig. 2). A rectangular ROI, approximately 300 pixels in height and 400 pixels in width (with slight variations depending on anatomy), was used to encompass the area under the teeth. The aBMD score at the mandibular angle was measured in a similar manner; however, this region typically exhibits lower aBMD values than the mandibular body,[8] thus providing a broader range of values.

Panoramic imaging is sensitive to patient positioning.[15] Common errors include placing the head outside the sharp focal layer, rolling the head to the left or right, or nodding forward or backward.[15-17] To evaluate the robustness of the aBMD measurements in the presence of minor positioning errors, phantom number 2 was subjected to several adjustments: it was nodded backward by 5°, moved upward by 2 cm while simultaneously being rolled to the right by 3°, and moved backward by 1 cm. These modifications were implemented while ensuring that the panoramic image remained interpretable (e.g., pulps of the teeth and mandibular canals were still visible). A control image was acquired under optimal positioning conditions.

Data acquisition

An experimental spectral photon counting panoramic system was used to image the phantoms. Specifically, the Planmeca Promax Mid system (Planmeca Oy, Helsinki,

Table 1. Spectral panoramic acquisition parameters

Parameters	Values
Source to image distance	60 cm
Tube voltage	70 kVp
Tube current	9 mA
Acquisition time	18 s
Dose-area product	72.1 mGy cm^2
Magnification	1.4
Field of view (width × height)	0.6 × 15.4 cm^2
Detector pixel size	0.1 × 0.1 mm^2
Detector energy thresholds	15, 36 keV

Finland) equipped with a DC-Vela detector (Varex Imaging Corporation, Salt Lake City, USA) was utilized. The DC-Vela is a photon-counting detector featuring 2 adjustable thresholds, charge-sharing correction, and a 0.75 mm cadmium telluride sensor layer. The acquisition parameters for this panoramic system are provided in Table 1.

A dual-source DECT scanner (SOMATOM Force, Siemens Healthineers, Erlangen, Germany) was employed to acquire dual-energy volumes. The MonoE+ protocol was used to generate virtual monoenergetic images of the scanned phantoms. Knowing the energy of the input images is criti-

Table 2. Dual-energy computed tomography acquisition parameters

Parameters	Values
Tube voltage	80/Sn150 kVp
Tube current	552/397 mA
Acquisition time	1 s
CTDIvol$_{16}$	49 mGy
Dose length product	1360 mGy cm
Monoe+	50/190 keV
Kernel	Qr69s/2
Axial voxel size	0.39 mm
Slice thickness	0.6 mm

cal for subsequent processing, as will be discussed in the following subsection. The acquisition parameters for the DECT system are listed in Table 2, and the Qr69 kernel was chosen to achieve the highest available spatial resolution.

Data processing

An algorithm for calibrating and decomposing data from a panoramic photon counting system was previously described.[13] Briefly, stationary calibration measurements were acquired using titanium and polyoxymethylene (POM) slabs of varying thicknesses. These materials were chosen because they are available in high purity and can be easily fabricated to the desired dimensions; titanium closely approximates the atomic number of calcium (and thus HAP), while POM has an effective atomic number similar to water and soft tissue.[18] The calibration measurements were used to generate virtual panoramic calibration images that match the dimensions of the panoramic acquisitions. A polynomial forward model was then calibrated via maximum likelihood estimation of model parameters for each pixel in the panoramic image. Subsequent panoramic images could be decomposed by applying regularized maximum likelihood estimation as if the image were a standard projection domain image.[19]

A simulation framework for generating synthetic spectral panoramic images from single-energy CT acquisitions was described in previous work.[14] In this approach, the initial segmentation step was replaced by an image-based material decomposition of the DECT data. Two virtual monoenergetic images served as input and were transformed into basis material images via matrix inversion. For water and dentin as basis materials, the decomposed image A is given by:

$$A = \begin{bmatrix} \mu_{ld} & \mu_{lw} \\ \mu_{hd} & \mu_{hw} \end{bmatrix}^{-1} I, \tag{1}$$

where μ represents the linear attenuation coefficients of the basis materials (d for dentin and w for water) at the monoenergetic energies (l for low and h for high), and I is a $2 \times i$ matrix (with i representing the number of voxels). The upper row of I contains the linearized voxel values from the low-energy monoenergetic volume, and the lower row contains the values from the high-energy volume. The resulting 2 material-decomposed images (the rows of A) were then incorporated into the previously described framework. Briefly, the dental arch was determined semi-automatically, a series of projections through the dental arch was generated for each decomposed volume, and panoramic reconstruction was subsequently performed. The resulting panoramic equivalent thickness images (PETIs) were used to calculate the aBMD scores.

Anatomical noise was estimated as described previously,[14] by recording the line-integral path lengths of each pixel in every projection that contributed to a given output pixel in the synthetic panoramic image. These recorded path lengths were then displayed as a histogram. Note that the synthetic image projections are noise-free, aside from the inherent noise of the DECT volume (which is minimal given the DECT dose and the post-processing applied). Adding noise to match experimental levels is not meaningful, as the synthetic images serve as the ground truth.

aBMD score calculation

A change of basis was applied to enhance the contrast between soft tissue and bone in the experimental material-decomposed panoramic images. Various basis material combinations were evaluated to identify the pair that minimized residual bone signal in the soft tissue image. Dentin and soft tissue emerged as the optimal combination. For synthetic panoramic images, dentin is the standard output. The aBMD values were calculated by multiplying the dentin image by the density of dentin (1.95 g/cm^3).[20]

For each ROI measurement site, 2 mean values were calculated: 1 for the mandible (excluding any overlap) and 1 for the background. The background mean was subtracted from the mandible mean to ensure comparability across different sites, as the background area in the hard tissue image is typically nonzero. Thresholding, combined with morphological operations (opening followed by closing), was used to segment the background and mandible and to exclude overlapping areas when necessary. The aBMD score for the Gammex inserts was calculated using the same method as for the anthropomorphic phantoms.

A linear fit between the synthetic and experimental mandible aBMD scores was performed with the intercept con-

strained to zero, based on the expectation that no intercept should exist between the 2 sets of values. The dataset comprised nine data points from 3 phantoms (left angle and both left and right bodies of the mandible). Given the small dataset, allowing a nonzero intercept would increase the risk of overfitting, and more complex relationships cannot be reliably estimated. The resulting fitting function was used to scale the experimental values to a magnitude comparable to the synthetic values.

Statistical analysis

Statistical analyses were performed using Python 3. Correlation coefficients and linear fits were computed using the NumPy package, while the root mean squared error (RMSE) was calculated using the scikit-learn package. The null hypothesis ($\rho = 0$) was tested by calculating the corresponding p-value with the SciPy package.

The RMSE for the anthropomorphic head phantoms was calculated to assess the deviation of the experimental values from the synthetic values, which were considered the ground truth. Pearson's correlation coefficient was computed for the anthropomorphic aBMD scores to evaluate the linearity between the synthetic and experimental measurements. Additionally, the correlation coefficient was calculated for the Gammex 472 dual-energy phantom inserts to verify the linearity of the measured aBMD values.

Results

Figure 2 presents the experimental material decomposition panoramic images for anthropomorphic phantom number 2. In the dentin image (Fig. 2A), prominent features include the maxilla, mandible, and teeth. However, the opposing mandible partially overlaps on both sides, and on the right side this overlap covers the mandibular angle, thereby precluding aBMD measurement at that location—a limitation observed in phantoms 1 and 3 as well. In the soft tissue image (Fig. 2B), the respiratory tract is the dominant feature, appearing as darker grooves. The dentin component exhibits a moderate negative correlation with the soft tissue
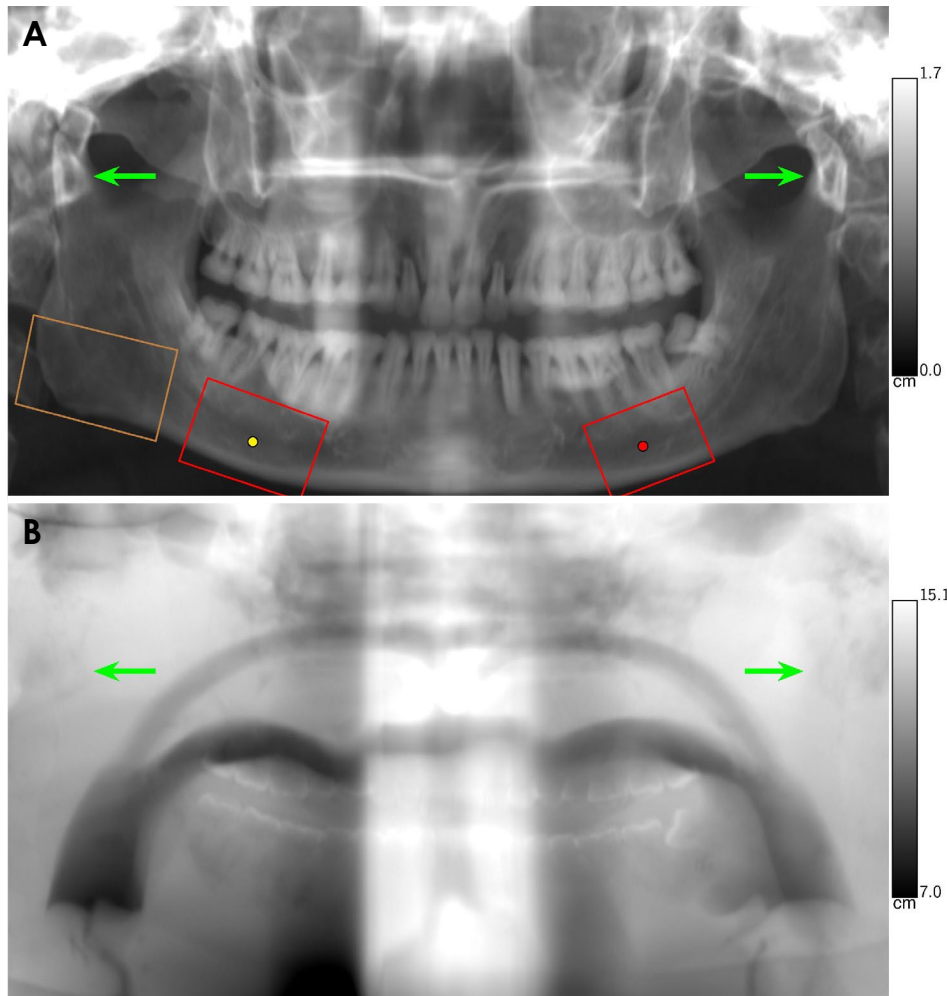
Fig. 3. A. Dentin image generated from a dual-energy computed tomography (DECT) scan using the simulation framework. Rectangles denote the areas used for aBMD measurement: red for the mandibular body and brown for the mandibular angle. Yellow (left) and red (right) dots indicate the anatomical noise measurement points. B. Soft tissue image obtained from a DECT scan using the simulation framework. Two examples of the weak inversely correlated signal from the dentin component in the soft tissue image are indicated by green arrows.

image; for instance, the teeth and mandibular base appear darker relative to the surrounding areas.

The synthetic panoramic images generated from DECT scans of anthropomorphic phantom number 2 are shown in Figure 3. As expected, the dentin component image (Fig. 3A) is dominated by bony features, with the mandible and teeth prominently visible in the lower half. The overlapping region of the mandible appears as wedges toward the center of the image, extending to the roots of the mandibular teeth. In the soft tissue component image (Fig. 3B), distinct features are visible: the respiratory tract appears as darker, arched lines, and the horizontal center—where more soft tissue is present—appears brighter than the edges. The dentin component imparts a very weak, inversely correlated signal to the soft tissue image (Fig. 3B), which is subtle. Additionally, the overlap between the cervical spine and the mandibular body manifests as a high-value region in the dentin image (Fig. 3A) and as a corresponding darker shape in the soft tissue image (Fig. 3B), as indicated by the arrows. Similar darker regions are observed where other bony features overlap. Notably, enamel, unlike other hard tissues, induces a positively correlated signal in the soft tissue image, making it appear brighter than the surrounding tissues.

The synthetic dentin component in Figure 3A closely resembles its experimental counterpart in Figure 2A in terms of feature contrast. For instance, the contrast among the mandibular base, the center of the mandibular body, and the roots of the teeth is similar in both images. However, the regions of mandibular overlap differ between the 2 images: in the synthetic image (Fig. 3A), these areas are narrow and centrally located, whereas in the experimental image (Fig. 2A) they are broader but less pronounced. This discrepancy likely arises from differences in the geometries used in the simulation compared to those in the experimental panoramic image generation. Nonetheless, the overall appearance of the teeth and mandible is consistent between the 2 sets of images.

Figure 4 presents the aBMD measurements for the 3 anthropomorphic phantoms. The linear fit between the experimental and synthetic values yielded a slope of 0.956, indicating that the absolute values from both approaches are very similar. The largest deviation observed was 0.06 g/cm^2 (approximately 9% in relative terms), and the low RMSE indicates a strong linear correlation.

The aBMD scores of phantom 2 at different positions are shown in Table 3. The RMSE on the left side was nearly identical to that shown in Figure 4, indicating that minor positioning errors did not increase the error. However, the RMSE on the right side was higher compared to Figure 4,
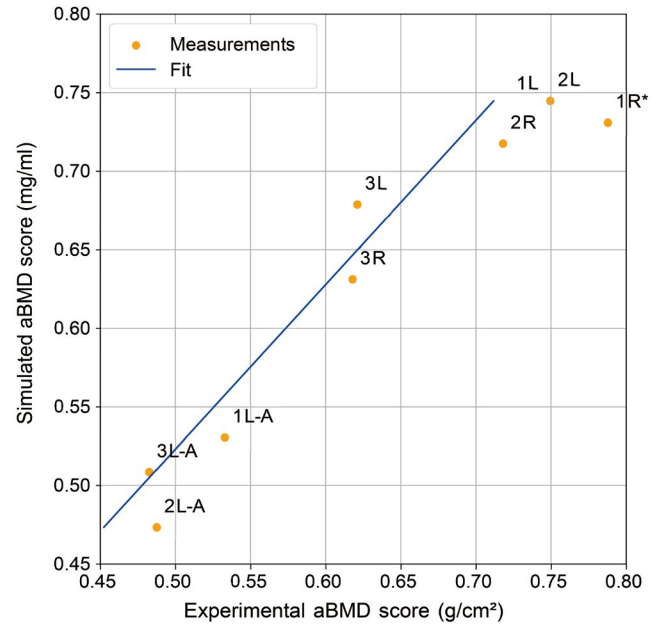

Fig. 4. Areal bone mineral density (aBMD) scores for phantoms 1-3, with scores provided for both sides (left or right) of the mandibular bodies and left angles (denoted as -A) of the mandible. An asterisk (*) indicates cases with significant overlap from the opposing mandible; only the non-overlapping area was used. Pearson correlation coefficient r = 0.969 (P < 0.001) and RMSE = 0.0292 g/cm^2.

Table 3. Areal bone mineral density (aBMD) scores for the mandibular body of phantom number 2 with different positioning errors (unit: g/cm^2)

Phantom position	Left	Right
Simulated measurement with optimal positioning	0.75	0.72
Control measurement at the correct position	0.79	0.74
Nodding backwards by 5°	0.74	0.81*
Moved up by 2 cm AND roll to the right by ≈3°	0.75	0.72
Moved back by ≈1 cm	0.78	0.75
Mean of the experimental measurements	0.764	0.752
Root mean squared error vs. simulated	0.0296	0.0474

*: significant overlap from the opposing mandible. Only the non-overlapping area was used.

which can be attributed to a single outlier—likely resulting from a reduction in the ROI area due to partial mandible overlap.

The results of the aBMD linearity test are shown in Figure 5. The experimental aBMD scores deviated by at most 0.13 g/cm^2 from the values predicted by the linear fit, and the correlation coefficient was nearly 1, indicating excellent linearity. It is noteworthy that the aBMD scores evaluated in the linearity test spanned a broader range (0.0 to 2.7 g/cm^2) compared to those from the anthropomorphic phantoms (0.5 to

$0.8\,\mathrm{g/cm}^2$ as shown in Fig. 4 and Table 3).

Figure 6 presents the anatomical noise histograms. The histogram counts at both measured points were very similar, indicating that the area used for aBMD measurements was anatomically stable; that is, the line-integral path lengths remained consistent regardless of angle or location within that area. Thus, the aBMD scores were not significantly affected by minor geometric variations or patient positioning errors.
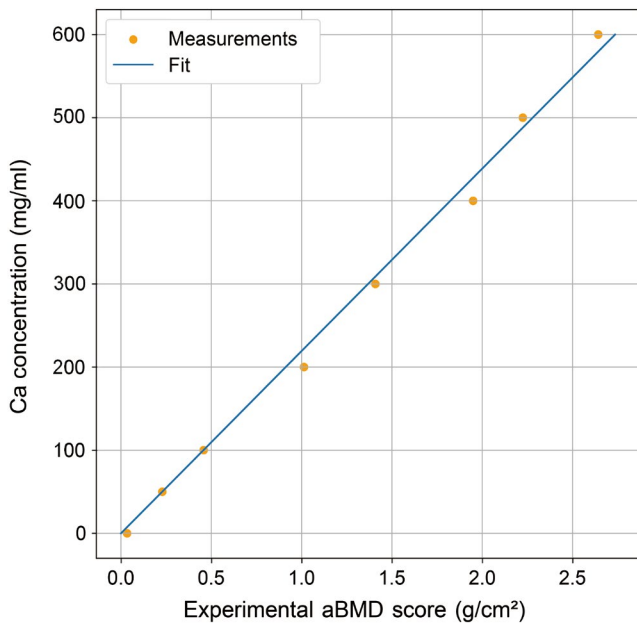

Fig. 5. Gammex calcium (Ca) inserts compared to the experimental areal bone mineral density (aBMD) scores, along with a linear fit. A Ca concentration of 0 mg/mL corresponds to the solid water insert. Pearson correlation coefficient r＝0.998 ($P<0.001$).

Discussion

This study demonstrated a method for generating mandibular aBMD scores using an experimental spectral panoramic imaging system. The method was validated by cross-verifying the results against gold-standard DECT data using a modified panoramic simulation framework. The visual similarity, consistent contrast, low RMSE, and high correlation between experimental and synthetic results collectively indicate that the aBMD scores obtained are reliable. Furthermore, the anatomical noise histograms in Figure 6 and the aBMD scores in Table 3 suggest that the method is robust against minor positioning or orientation errors.

The main results, shown in Figures 4 and 5, exhibit very high correlation coefficients with P-values <0.001, indicating statistical significance despite some imperfections in the regression. The correlation in Figure 4 is slightly lower than that in Figure 5, which can be attributed to the fact that, if the noise magnitude is similar for both datasets (due to matching dose and attenuation), the relative deviation will be more pronounced when the range of values is narrower, as seen in Figure 4.

One discrepancy between the experimental and synthetic images is that enamel produces a negatively correlated soft tissue signal in the experimental image, similar to other bony tissues, but a positively correlated signal in the synthetic image. The positive correlation observed for enamel is likely an artifact, since it is counterintuitive that the most attenuating tissue would generate a positive signal on another spectral channel. A probable explanation is a partial volume effect, whereby the thin dentin layer's attenuation is blended with the attenuation of the surrounding plastic. Confirma-
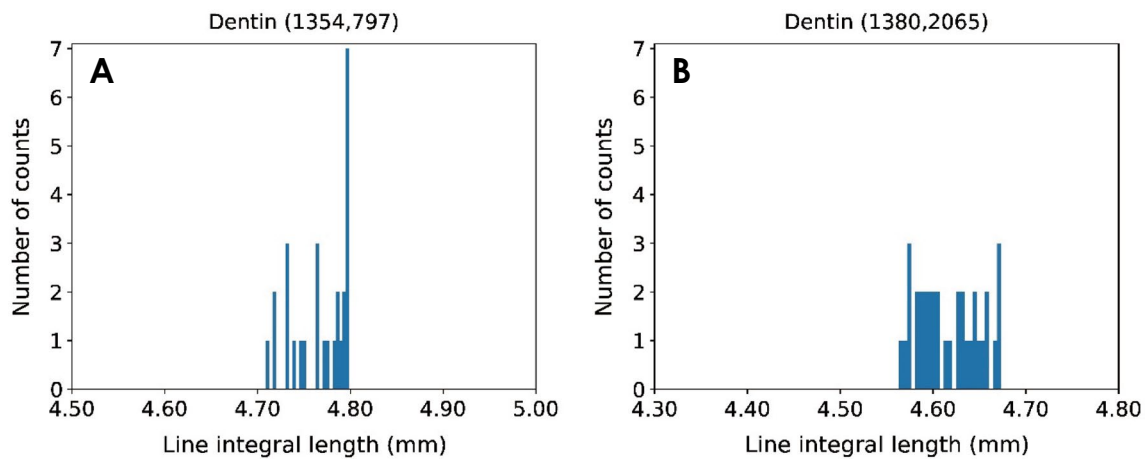

Fig. 6. Anatomical noise histograms for the synthetic dentin image in Figure 3A, with pixel indices in the label. The yellow point in Figure 3 corresponds to histogram A and the red point to histogram B. Both histograms have counts only in a very narrow range of line-integral lengths.

tion of this effect would require a high-resolution spectral imaging system, such as a photon counting CT.[21]

The overlap of the opposing mandible in the experimental images introduced challenges in determining aBMD scores, particularly by preventing measurements at the right mandibular angle. This overlap is most likely due to suboptimal detector mounting. Future improvements in detector mounting are expected to reduce the overlap region, ensuring that it does not encroach upon the aBMD measurement area. Despite this limitation, the aBMD scores were in good agreement overall.

The ROIs used for aBMD measurements in Figure 4 and Table 3 were selected manually, which may lead to slight mismatches between the experimental and synthetic images and introduce potential errors. Automatic segmentation and registration of the mandible could mitigate this issue.[22] Additionally, quantum noise is amplified during the decomposition process.[23] Although regularization reduces this noise, it does not completely eliminate it, contributing some variance to the results.

Ideally, scaling the experimental aBMD scores to match the synthetic ones would not be necessary. However, in the experimental setup, a change of basis is required to convert calibration materials into physically meaningful materials (soft tissue and dentin). This difference in generating the synthetic and experimental dentin images is a potential source of error in comparing aBMD scores. If DECT values are accepted as the ground truth, tuning the basis vector energies might improve the match between experimental and synthetic results. Nevertheless, perfect regression between the 2 datasets is unlikely, as the imaging systems and settings differ—one employing image-domain decomposition and the other using projection-domain decomposition—and they are subject to varying degrees of scatter.

In lumbar spine DXA measurements, a reference score is established based on age, sex, and body mass index.[24] To determine whether a similar scaling approach is necessary for spectral panoramic mandibular aBMD scores, an *in vivo* patient study with a substantial sample size is warranted.

Despite the limitations discussed, the synthetic and experimental panoramic images show strong agreement. This suggests that it is technically feasible to employ spectral panoramic imaging for osteoporosis and periodontal disease screening via aBMD measurements without increasing patient radiation exposure. Additionally, orthodontics could benefit from the ability to measure aBMD scores of specific teeth and surrounding tissues before and after implant placement, although mandible overlap may pose challenges in certain cases. Given that panoramic imaging is the most

common extraoral dental radiological examination,[12] the clinical potential of this approach is substantial.

Conflicts of Interest: VS is an employee of Planmeca Oy. YH, TP; and HL are employees of Varex Imaging Corporation. The remaining authors declare no conflicts of interest.

References

1. Lin JT, Lane JM. Osteoporosis: a review. Clin Orthop Relat Res 2004; 425: 126-34.
2. Riggs BL, Melton LJ 3rd. The worldwide problem of osteoporosis: insights afforded by epidemiology. Bone 1995; 17(5 Suppl): 505S-11.
3. Lewiecki E, Chastek B, Sundquist K, Williams SA, Weiss RJ, Wang Y, et al. Osteoporotic fracture trends in a population of US managed care enrollees from 2007 to 2017. Osteoporos Int 2020; 31: 1299-304.
4. Giro G, Chambrone L, Goldstein A, Rodrigues JA, Zenóbio E, Feres M, et al. Impact of osteoporosis in dental implants: a systematic review. World J Orthop 2015; 6: 311-5.
5. Von Wowern N, Klausen B, Kollerup G. Osteoporosis: a risk factor in periodontal disease. J Periodontol 1994; 65: 1134-8.
6. Von Wowern N. General and oral aspects of osteoporosis: a review. Clin Oral Investig 2001; 5: 71-82.
7. Blake GM, Fogelman I. Technical principles of dual energy X-ray absorptiometry. Semin Nucl Med 1997; 27: 210-28.
8. Horner K, Devlin H, Alsop CW, Hodgkinson IM, Adams JE. Mandibular bone mineral density as a predictor of skeletal osteoporosis. Br J Radiol 1996; 69: 1019-25.
9. Calciolari E, Donos N, Park JC, Petrie A, Mardas N. A systematic review on the correlation between skeletal and jawbone mineral density in osteoporotic subjects. Clin Oral Implants Res 2016; 27: 433-42.
10. Bozic M, Ihan Hren N. Osteoporosis and mandibles. Dentomaxillofac Radiol 2006; 35: 178-84.
11. Fahrig R, Jaffray DA, Sechopoulos I, Webster Stayman J. Flat-panel conebeam CT in the clinic: history and current state. J Med Imaging (Bellingham) 2021; 8: 052115.
12. United Nations. Sources, effects and risks of ionizing radiation. UNSCEAR 2020/2021. Report to the general assembly, with scientific annexes [Internet]. New York: United Nations; 1994 [cited 2024 Nov 11]. Available from https://www.unscear.org/unscear/uploads/documents/unscear-reports/UNSCEAR_2020_21_Report_Vol.I.pdf.
13. Somerkivi V, Sellerer T, Pantsar T, Lohman H, Pfeiffer F. Spectral photon counting for panoramic dental imaging. Biomed Phys Eng Express 2023; 9: 035017.
14. Somerkivi V, Kolb A, Sellerer T, Berthe D, Haemisch Y, Pantsar T, et al. Generating spectral dental panoramic images from computed tomography volumes [Internet]. arXiv 2023; 2305.10087 [cited 2024 Nov 11]. Available from https://arxiv.org/abs/2305.10087.
15. Rondon RHN, Pereira YC, do Nascimento GC. Common positioning errors in panoramic radiography: a review. Imaging Sci Dent 2014; 44: 1-6.

16. Kaviani F, Johari M, Esmaeili F. Evaluation of common errors of panoramic radiographs in Tabriz faculty of dentistry. J Dent Res Dent Clin Dent Prospects 2008; 2: 99-101.

17. Dhillon M, Raju SM, Verma S, Tomar D, Mohan RS, Lakhanpal M, et al. Positioning errors and quality assessment in panoramic radiography. Imaging Sci Dent 2012; 42: 207-12.

18. Hubbell J, Seltzer S. Tables of X-ray mass attenuation coefficients and mass energy-absorption coefficients 1 keV to 20 MeV for elements Z = 1 to 92 and 48 additional substances of dosimetric interest [Internet]. Gaithersburg: Radiation Physics Division, PML, NIST; c1989, 1990, 1996 [cited 2025 Nov 11]. Available from https://www.nist.gov/pml/x-ray-mass-attenuation-coefficients.

19. Mechlem K, Sellerer T, Ehn S, Munzel D, Braig E, Herzen J, et al. Spectral angiography material decomposition using an empirical forward model and a dictionary-based regularization. IEEE Trans Med Imaging 2018; 37: 2298-309.

20. Gradl R, Zanette I, Ruiz-Yaniz M, Dierolf M, Rack A, Zaslansky P, et al. Mass density measurement of mineralized tissue with grating-based X-ray phase tomography. PLoS One 2016; 11: e0167797.

21. Thomsen FS, Horstmeier S, Niehoff JH, Peña JA, Borggrefe J. Effective spatial resolution of photon counting CT for imaging of trabecular structures is superior to conventional clinical CT and similar to high-resolution peripheral CT. Invest Radiol 2022; 57: 620-6.

22. Abdi AH, Kasaei S, Mehdizadeh M. Automatic segmentation of mandible in panoramic X-ray. J Med Imaging (Bellingham) 2015; 2: 044003.

23. Mechlem K, Ehn S, Sellerer T, Braig E, Munzel D, Pfeiffer F, et al. Joint statistical iterative material image reconstruction for spectral computed tomography using a semi-empirical forward model. IEEE Trans Med Imaging 2018; 37: 68-80.

24. Dimai HP. Use of dual-energy X-ray absorptiometry (DXA) for diagnosis and fracture risk assessment; WHO-criteria, T- and Z-score, and reference databases. Bone 2017; 104: 39-43.